Int. J. Electrochem. Sci., 15 **(2020)** 613 – 627, doi: 10.20964/2020.01.58

International Journal of
ELECTROCHEMICAL
SCIENCE
www.electrochemsci.org

Air Bleeding Strategies to Increase the Efficiency of Proton Exchange Membrane Fuel Cell Stationary Applications Fuelled with CO ppm-levels

*S. Delgado, T. Lagarteira and A. Mendes**

Laboratory for Process Engineering, Environmental, Biotechnology and Energy (LEPABE), Faculty of Engineering of University of Porto, Rua Dr. Roberto Frias s/n, 4200-465 Porto, Portugal
*E-mail: mendes@fe.up.pt;

Received: 12 August 2019 / *Accepted:* 28 September 2019 / *Published:* 30 November 2019

The use of proton exchange membrane fuel cells (PEMFCs) as efficient electric generators for residential and tertiary sectors to replace conventional internal combustion engines greatly depends on the recent advances in purification technologies. Preferential oxidation and pressure swing adsorption offer reformate hydrogen streams with CO concentrations down to fractional ppm level. However, even small traces of CO cause reversible and irreversible performance losses of the PEMFC stack due to poisoning of the anode Pt catalyst. This work reports the performance loss upon H_2 contamination down to the ppm level and the efficiency gains after applying internal and external air bleeding to the anode of the fuel cell. This work studies both air bleeding strategies under operating conditions typical for stationary applications. By adding solely 1 % of air bleed to a 10 ppm CO contaminated hydrogen stream, it is possible to recover the full performance without compromising the steadiness of the cell. Moreover, a performance loss of < 1 % – DOE target value for reformate streams – can be met using Pt-Ru based anode catalysts allied to a minimal air bleed concentration. Long-term experiments, *ca.* 80 h, were performed to assess the stability of the fuel cells fed with contaminated hydrogen and compare the long-term impacts of both internal and external air bleeding.

Keywords: Proton exchange membrane fuel cell; Membrane electrodes assembly; CO poisoning; Air bleeding.

1. INTRODUCTION

Low-temperature proton exchange membrane fuel cells (PEMFCs) are considered an attractive candidate to power small stationary units including off-grid energy, backup power systems and combined heat and power (CHP) for industry and buildings. CHP systems based on fuel cells are expected to replace natural gas heaters for domestic cogeneration, because of their higher fuel efficiency, modularity, and environmentally friendly operation [1]. However, some challenges still hinder the widespread commercialization of the technology. The core component of the fuel cell, the membrane-electrodes assembly (MEA), plays a crucial role on the overall cost of fuel stacks due to the need of highly active and durable catalysts and electrodes. In parallel to the high cost of the precious-metal catalysts, the small world-wide production of highly pure hydrogen is a major drawback [2].

Systems for stationary applications usually adopt a fuel processor to produce hydrogen from fossil (natural gas, LPG) or renewable (bio-ethanol, bio-gas) fuels [3]. The reforming of hydrocarbons followed by water-gas shift and purification is the most common production route of hydrogen. Nonetheless, this production route still delivering contaminants (CO_2, H_2S and mainly CO) in the hydrogen stream that poison platinum catalyst activity and durability [4,5]. Therefore, ISO 14687-3 details hydrogen quality requirements for PEM fuel cells for stationary applications. In particular, it defines three categories: two with $H_2 \geq 50$ % and CO ≤ 10 ppm, and one with $H_2 \geq 99.9$ % and CO ≤ 0.2 ppm. Hydrogen produced by conventional fuel processors can fulfil the requirements of the first two categories. Japan appears as the world leader on micro-combined heat and power systems based on fuel cells (m-CHP-PEMFC) for buildings with over 140 000 units sold; likewise, Europe is expected to promote the exponential growing of m-CHP-PEMFC [6,7]. The chemisorption of CO on Pt catalyst particles surface reduces the number of active sites for H_2 electro-oxidation [8,9] and hence the fuel cell power output and its useful life. The performance of the fuel cell anode is then highly sensitive to small traces of CO (down to fractional ppm level) and dependent on operating conditions such as temperature, the exposure time to CO, pressure, current density, relative humidity and fuel stoichiometry [10]. Carbon dioxide has a minimal affinity for the Pt catalyst and therefore does not affect the performance of the cell at low current densities (< 300 mA cm^{-2}), behaving as an inert species [11].

In the last two decades, several works have been published focusing on the mitigation of CO poisoning in PEM fuel cells [10,12–14]. The most conventional approach is to use CO-tolerant catalysts at the anode, normally obtained by combining Pt with other metals. Pt-Ru alloy is typically used as CO-tolerant catalyst albeit some impact on the fuel cell durability due to Ru dissolution and migration to the cathode [15,16]. The CO tolerance evidenced by PtRu catalysts is mainly attributed to two mechanisms, the electronic tuning of Pt d-band structure (ligand effect) and/or the acceleration of CO oxidation to CO_2 by providing oxygen species to CO_{ad} on Pt surfaces [17]. The ligand effect consists in the modification of Pt electronic structure that either weakens the Pt-CO bond thus promoting CO oxidation by nearby OH groups; or improves Pt-H_2O activation that leads to direct oxidation of CO on the Pt sites [18].

Another approach to inhibit CO poisoning is to introduce trace concentrations of oxygen in the anode. Oxygen can be supplied to the anode by: i) internal oxygen/air bleeding from the cathode through the membrane; ii) external oxygen/air bleeding; iii) introduction of H_2O_2 in the anode bubbler [10]. Oxygen permeation through the membrane is commonly described in terms of sorption-diffusion mechanisms [19]; specifically, during PEMFC operation oxygen sorbs into the membrane and diffuses from the cathode to the anode side preferably through its hydrated pathways. The membrane permeability to oxygen is proportional to the product of Fick's diffusion coefficient and solubility coefficient [20],[21]. The membrane permeability to oxygen increases with the operating temperature and with the membrane humidification [22–25]. On the other hand, oxygen permeation increases with the partial pressure difference between the two sides of the membrane but decreases with increasing membrane thickness [26]. The permeated oxygen is partly responsible for the oxidation of CO to CO_2 in the anode catalyst particles surface through heterogeneous catalysis described by the Langmuir-Hinshelwood mechanism [27]. Yet, some negative aspects may arise from the presence of excessive O_2 at the anode such as higher anode overpotential caused by water production from the hydrogen oxidation, catalyst sintering due to the highly exothermic hydrogen oxidation, and membrane degradation from the side-production of H_2O_2 [16]. Therefore, air (oxygen) bleeding must be tuned depending on the CO contamination levels [28].

In this work, the impacts of two different techniques for the mitigation of CO poisoning, internal and external air bleeding, are assessed. For both techniques, oxygen traces at the anode were tuned to determine the minimum amount able to fully recover the efficiency drop caused by CO poisoning. Mid-term operation under CO contamination was compared for both techniques to assess the degradation through potential decay. To the best of the authors' knowledge, these techniques are compared for the first time under PEMFC operating conditions suitable for stationary applications, such as m-CHP-PEMFC.

2. EXPERIMENTAL

The electrochemical measurements were carried out in a 25 cm^2 fuel cell manufactured by Pragma Industries. The graphite flow fields used in both the anode and cathode were single channel type. The cell compression was set to *ca.* 2 MPa, thus guaranteeing the electrical contact between the gas diffusion electrodes (GDE) and the bipolar plates.

MEA#1 was made of a Nafion 212 membrane (N212, 51 μm of thickness) sandwiched by two GDEs, all purchased to Quintech. The anode catalyst layer contained 0.5 mg cm^{-2} of PtRu and the cathode catalyst layer had 0.5 mg cm^{-2} of Pt. The GDEs were hot-pressed to the membrane at 120 °C and 17 bar for 5 minutes. The French Alternative Energies and Atomic Energy Commission (CEA) provided MEA#2 that employs a Nafion reinforced-stabilized HP membrane (NRHP) with 22 μm of thickness. The catalyst layers contained 0.585 mg cm^{-2} of PtRu (66 wt.% of Pt) in the anode and PtCo alloy with 0.468 mg cm^{-2} of Pt in the cathode. The gas diffusion layers of both MEAs (Sigracet 28 BC, SGL Carbon) were 220 μm thick.

The mass flow rates of the reactants, humidification and temperatures of the lines were controlled with a test station. The anode was fed with either high purity H_2 (99.999 %), mixtures of CO/H_2 or synthetic air whilst the cathode was fed with synthetic air. CO was supplied from a cylinder containing a mixture of H_2 balanced with 100 ppm of CO (Linde). Anode and cathode were humidified by bubbling the feed gases into ultra-pure water; the relative humidity was set to 50 % for both the anode and cathode. The stoichiometries of the reactants were set to 1.5/2 for the anode and cathode, respectively. Subsequently, the consumed reactant flow rates were calculated using Faraday's equation, assuming a coulombic efficiency of 100 %.

An electrochemical workstation (Zahner IM6eX) coupled with a PP-240 power potentiostat was used to perform the electrochemical measurements. The MEAs were subjected to break-in at 500 mA cm^{-2}. The conditions for the break-in and experiments of interest are described in Table 1. The break-in step (conditions of Run# 1) was considered completed when the cell potential variation was less than 5 mV h^{-1} at 500 mA cm^{-2}.

After achieving steady-state performance, a polarization curve was recorded in galvanostatic mode. The cell potential was recorded (Run# 2) as a function of the current density with a dwell time of 3 minutes. Chronopotentiometries were performed at 500 mA cm^{-2} following the conditions of Run #2-Run #10 to evaluate the magnitude of performance loss due to CO exposure and the performance gains after implementing each bleeding technique.

Electrochemical impedance spectroscopy (EIS) was performed in galvanostatic mode at 500 mA cm^{-2}, with a perturbation amplitude of 40 mA cm^{-2} between 10 kHz and 100 mHz.

Figure 1 depicts the equivalent circuit of elements used to fit the electrochemical impedance spectra. The equivalent circuit chosen comprises two simple Randle's circuits, each with a constant phase element ($Q_{a/c}$) and a resistor ($R_{a/c}$) in parallel, along with a resistor connected in series (R_m) [29]. R_m accounts mostly for the resistance associated to protonic conduction through the membrane, R_a and R_c are the charge transfer resistances associated to anode and cathode, respectively. EIS low frequency data, related to mass transfer overpotential, was not included in the fittings since it was not preponderant for this study.

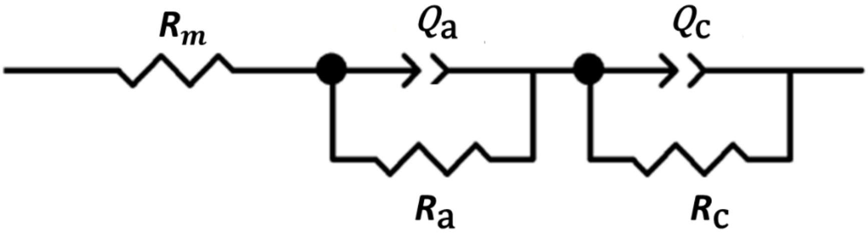

Figure 1. Schematic representation of the equivalent circuit for the PEMFC.

In-situ cyclic voltammetry (CV) was performed to both anode and cathode of the MEAs to estimate the electrochemical surface area (ECSA) at the beginning and end of experiments. The working electrode was purged with N_2 to remove any adsorbed O_2, and the counter electrode was fed with H_2, maintaining the stoichiometry and flow rates calculated for 100 mA cm^{-2} between H_2/O_2. The relative humidity was set to 50 %, the back pressure was set to 1.5 bar for both electrodes, the scan rate was set to 50 mV s^{-1} and the cell temperature was kept at 70 °C.

Table 1. Performed tests and corresponding operating conditions.

#	**MEA#**	***p* H_2**	***p* Air**	**RH H_2**	**RH Air**	**Fuel**	**Temperature**
1 – Break-in	1 / 2	1.5	1.5	80 %	80 %	Pure H_2	80 °C
2 - Reference	1 / 2	1.2	1.2	50 %	50 %	Pure H_2	70 °C

3	1 / 2	1.2	1.2	50 %	50 %	H_2 + 10 ppm CO	70 °C
4	1 / 2	1.1	1.2	50 %	50 %	H_2 + 10 ppm CO	70 °C
5	1 / 2	1.1	1.3	50 %	50 %	H_2 + 10 ppm CO	70 °C
6	2	1.1	1.3	50 %	50 %	H_2 + 20 ppm CO	70 °C
7	2	1.1	1.3	50 %	50 %	H_2 + 30 ppm CO	70 °C
8	1	1.2	1.2	50 %	50 %	H_2 + 10 ppm CO + 0.5 % Air	70 °C
9	1 / 2	1.2	1.2	50 %	50 %	H_2 + 10 ppm CO + 1 % Air	70 °C
10	1	1.2	1.2	50 %	50 %	H_2 + 10 ppm CO + 1.5 % Air	70 °C

3. RESULTS AND DISCUSSION

3.1. Electrochemical performance with pure H_2

The polarization curves (Figure 2a) and EIS spectra at 500 mA cm^{-2} (Figure 2b) of MEA#1 and MEA#2 were obtained for Reference conditions –Table 1. MEA#2 outperformed MEA#1 at current densities higher than 300 mA·cm^{-2}. The greater thickness of membrane N212, inserted in MEA#1, compared with membrane NRHP, inserted in MEA#2, makes its ohmic overpotential higher, limiting the protonic conduction and decreasing the power output [30]. Nafion HP is a sandwich type membrane, similar to its predecessor Nafion XL (*ca*. 28 µm), comprising an inner layer of PTFE-rich reinforcing mesh for mechanical stability, coated with two ultra-thin layers of Nafion in each side (ca. 7 µm thick each). This membrane provides high proton conductivity with better chemical/mechanical durability compared to the benchmark counterparts (*e.g.* Nafion 212 or Nafion 115) [31–33]. Nonetheless, the activation overpotential region (< 100 mA·cm^{-2}) of MEA#2 is higher comparing to MEA#1, thanks to the higher Pt loading of the latter. Nevertheless, ohmic overpotentials are smaller for MEA#2 (Figure 2a). From the EIS spectra (Figure 2b), the difference in the ohmic resistances of MEA#2 and MEA#1 – 107.4 mΩ cm^2 vs 221.4 mΩ cm^2, respectively – was assigned to the membranes thickness where MEA#2 is equipped with a membrane *ca*. 50 % thinner (22 µm) than MEA#1 (51 µm); these results are in line with previous studies [34,35]. Ohmic losses tend to increase linearly with membrane thickness [36]. Additionally, the lower mass transport overpotential of MEA#2 suggests the existence of more gas and liquid diffusion-pathways in the cathode catalyst layer.

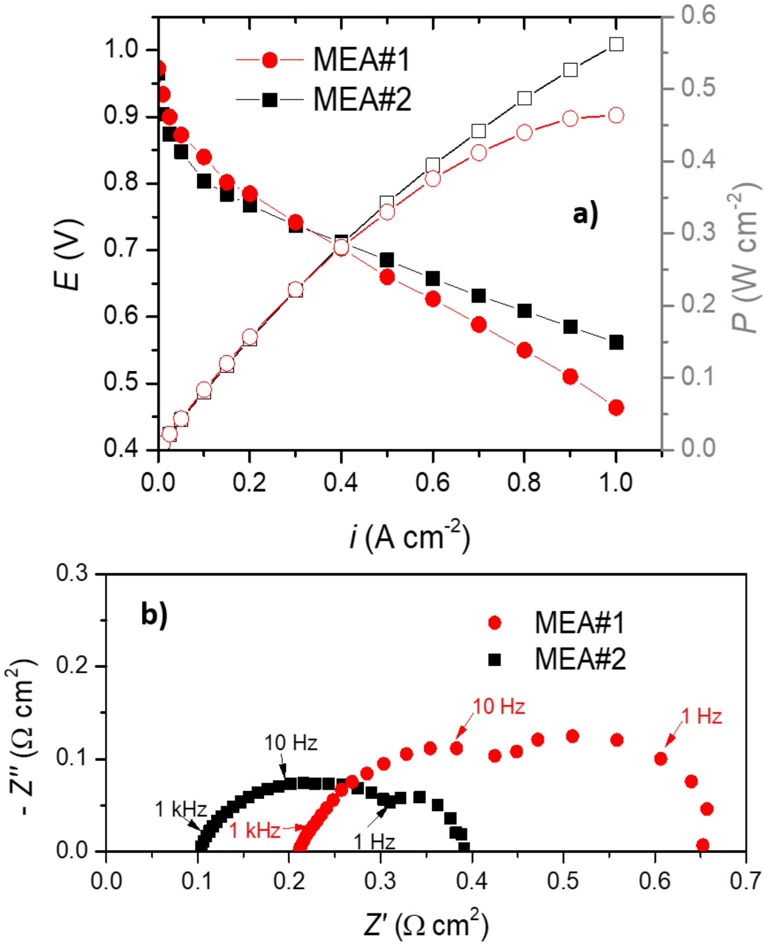

Figure 2. Comparison between the two tested MEAs under the conditions of Run#2 (from Table 1.) by a) a polarization curve; b) EIS at 500 mA·cm^{-2}.

Hereafter both MEA#1 and MEA#2 will assess the defined strategies to mitigate CO contamination – internal and air bleeding – under the operating conditions shown in Table 1. Runs #3 - #13.

3.2. Internal air bleeding

Internal air bleeding was controlled by setting a pressure difference between the two electrodes. The solubility of oxygen in water, which controls the oxygen transport to the anode, is related to its partial pressure. Therefore, the cathode side pressure must be higher to promote oxygen permeation through the membrane [26]. Error! Reference source not found.**a** shows chronopotentiometries of MEA#1, at 500 mA cm^{-2}, for pure hydrogen feed (Run #2) and for hydrogen with 10 ppm of CO feed (Runs #3, #4 and #5). With the introduction of CO at the anode, a linear loss of cell potential was observed until reaching a new steady-state. The effect of the internal air bleeding was not evident up to 0.1 bar of pressure difference. At 0.2 bar of cathode over-pressure, the steady-state cell potential increased *ca.* 20 mV, denoting a partial recovery of catalyst poisoning by CO, *ca.* 51 %.

The impedance spectra obtained at 500 mA cm^{-2}, were fitted to an EC shown in

Figure 1 to better diagnose the effect of the CO poisoning mitigation strategies. From the EIS spectra (Figure 3b), in the high-frequency region the anodic charge transfer resistance increased significantly when CO was fed with no internal bleeding – R_a = 67.8 mΩ cm^2 vs R_a =120 mΩ cm^2. When an internal bleeding is employed, Δ*P* = 0.2 bar, the anodic charge transfer resistance decreased significantly, R_a = 82.9 mΩ cm^2 (Table 2).

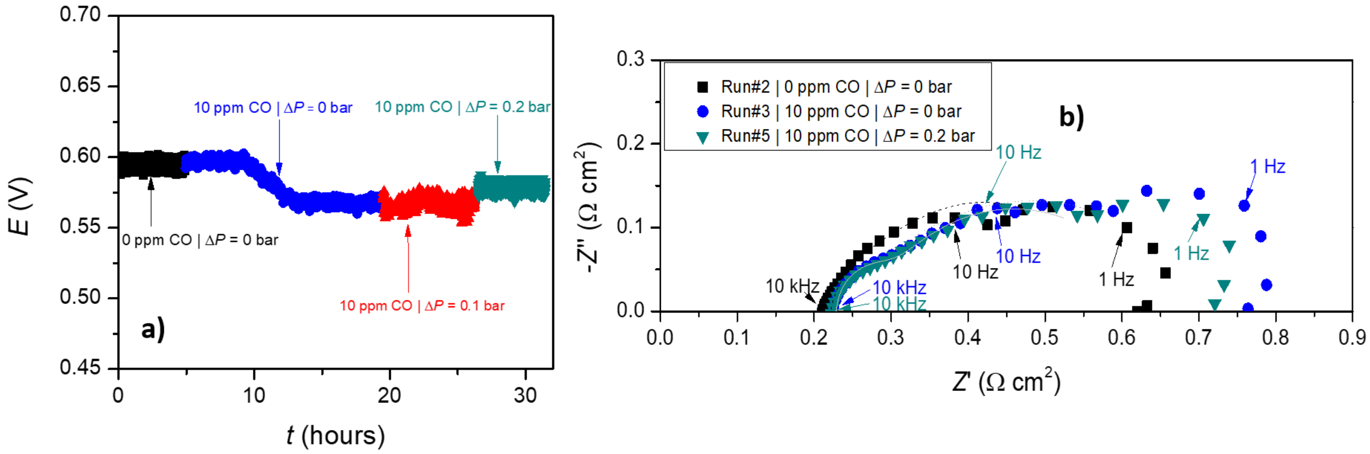

Figure 3. Effect of internal air bleeding on a) chronopotentiometry and b) EIS at 500 mA cm^{-2} of MEA#1.

Table 2. Summary of fitted values from EIS data using the equivalent circuit shown in Figure 1 for MEA#1 and#2; (Frequency range of the EIS fitted data: 2.5 kHz – 10 Hz).

MEA	**#**	***Rm* / mΩ cm^2**	***Ra* / mΩ cm^2**	***Q_a* / F cm^2**	***Rc* / mΩ cm^2**	***Q_c* / F cm^2**
1	**2 -** 0 ppm CO	221.4	67.8	639 m	293.2	789 m
	3 - 10 ppm CO	243	117.7	294 m	347.5	443.8 m
	5 - 10 ppm CO | Δ*P* =0.2 bar	233.2	82.9	146.9 m	326.5	254.9 m
	10 - 10 ppm CO + 1.5% air bleed	213.1	67.5	681.5 m	278.3	790.5 m
2	**2 -** 0 ppm CO	107.4	49.5	16.1	174	23.7
	3 - 10 ppm CO	125.4	237.4	11	315.8	6.3
	5 - 10 ppm CO | Δ*P*=0.2 bar	122.5	224.3	7.9	252.5	9.4
	9 - 10 ppm CO + 1% air bleed	109.4	44.6	15.6	160.7	22.4

Runs #2, #3, #4 and #5 were repeated with MEA#2. Figure 4**a** displays the chronopotentiometries of MEA#2 at 500 mA cm^{-2}. After CO contamination, the steady-state cell potential increased with the cathode over-pressure (*ca.* 10 ± 2 mV per 0.1 bar). Therefore, internal air bleeding effect is hardly noticeable in EIS (Figure 4**b**), since the spectra of Runs #3 and #5 almost overlap. Moreover, .the effect of internal air bleeding with an over-pressure of 0.2 bar allows a recovery of 25 % of the pristine performance and a reduction of anode charge transfer resistance of *ca.* 10 mΩ cm^2, comparing with Run #3, according to the EIS fitting - **Table 2**.

Oxygen bleeding on several membranes has been a subject of several studies, which report that CO poisoning mitigation is lower for thicker membranes like Nafion 115 (127 µm) [27]; the work of Wang [37] reported higher oxygen bleeding when the cathode over-pressure increases in ultra-thin membranes (5 µm and 25 µm). These evidences support that performing internal bleeding for CO poisoning mitigation is more effective if thin membranes are used. By promoting back diffusion of water dissolved oxygen through thin membranes (internal bleeding), more CO present at the anode can be oxidized to CO_2, thus reducing the anode overpotential caused by CO poisoning. Increments on the cathode total pressure promotes CO oxidation [37] but only *ca*. 0.25 % of the crossed oxygen molecules oxidize CO to CO_2 [37]. In the present study, a similar performance gain was achieved for both MEA#1 and MEA#2, as seen in Figure 3a and Figure 4b. Nonetheless, no more than 40 % of the initial performance could be re-established; pressure gradients higher than 200 mbar between the electrodes were not employed to avoid high mechanical stress that could lead to form pin-holes in the membrane and consequent gas crossover or internal short-circuits.

There is no agreement whether Nafion-PTFE composite membranes display better gas barrier properties compared with plain Nafion membranes (*e.g.* Nafion 115, Nafion 117 among others); several works [38–40] report greater permeabilities of Nafion/PTFE composite membranes to oxygen and nitrogen. The PTFE mesh in the composite membrane allows to reduce the overall membrane thickness (from typical *ca.* 185 µm -Nafion 117 - to less than 40 µm) while keeping the mechanical stability. These authors observed higher composite membrane permeabilities to gas relatively to thicker non-reinforced membranes [41]. On the other hand, Yu and his co-workers developed a Nafion/PTFE composite with an overall thickness of 20 ± 5 µm and, upon scanning electron microscopy analysis, they confirmed that PTFE pores were completely filled with the Nafion resin. The permeability of the composite membrane to nitrogen was reduced when comparing to non-reinforced Nafion 112, 115 or 117 [39].

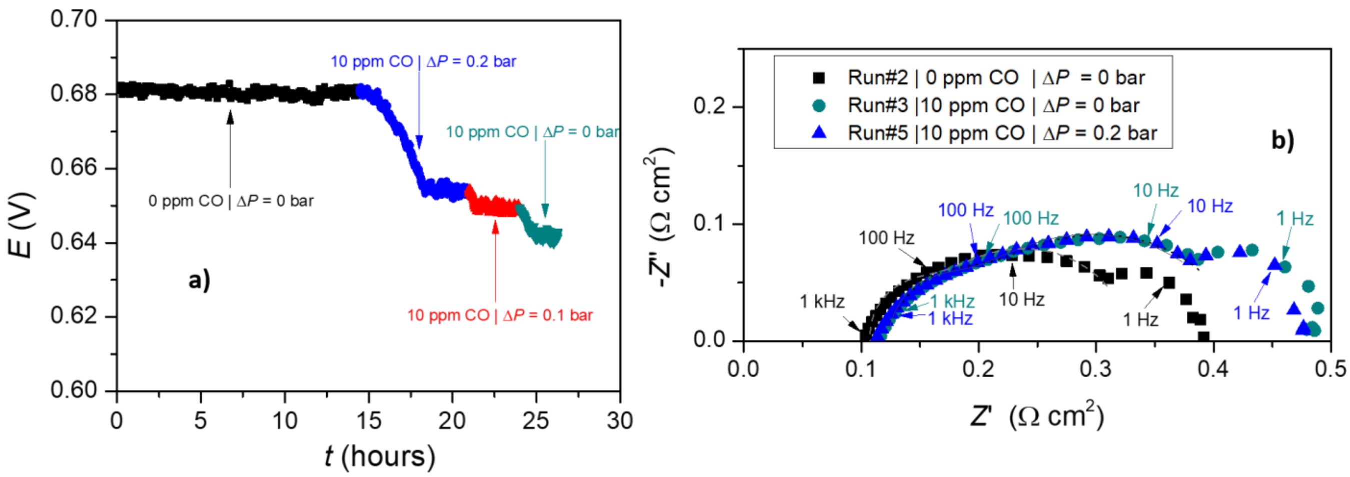

Figure 4. Effect of internal bleeding in MEA#2 at 500 mA·cm^{-2} on a) chronopotentiometry and b) EIS.

In the present study, the use of a thinner membrane (Nafion HP in MEA#2) did not provide better internal bleeding-based performance recovery than thicker Nafion 212 membrane (MEA#1). Nafion HP membranes are reinforced with a backbone that makes them not only mechanically more stable but also less permeable to both hydrogen and oxygen. The lower permeability to oxygen limits internal bleeding and thus CO mitigation is less effective comparing to non-reinforced membranes of similar thickness.

Higher concentrations of CO in the fuel stream were also tested together with internal bleeding. The pressure difference between cathode and anode was set to 200 mbar to enable internal air bleeding under different CO contaminations. Figure 5a shows the chronopotentiometries for four levels of CO contamination (0, 10, 20 and 30 ppm). The efficiency of the cell provided with MEA#1 at 500 mA cm^{-2} and 80 °C fell from the initial value of 45.2 % while feeding neat H_2 to progressively lower efficiencies, *ca*. - 0.55 % with each increase of 10 ppm of CO. In this regard, the steady state potential decreased with the CO concentration, mainly because of increasing anode overpotential.

The impedance spectra (Figure 5b), obtained after each chronopotentiometry, unveils that higher CO concentrations increase the overall impedance. The differences are clear for frequencies lower than 1 Hz, where gradual increments of 10 ppm in the CO concentration originate two-fold higher anode charge transfer resistances, *i.e.*, the resistance increases *ca.* 20 mΩ cm^2 when CO passes from 10 ppm to 20 ppm, and *ca.* 40 mΩ cm^2 when passing from 20 ppm and 30 ppm of CO.

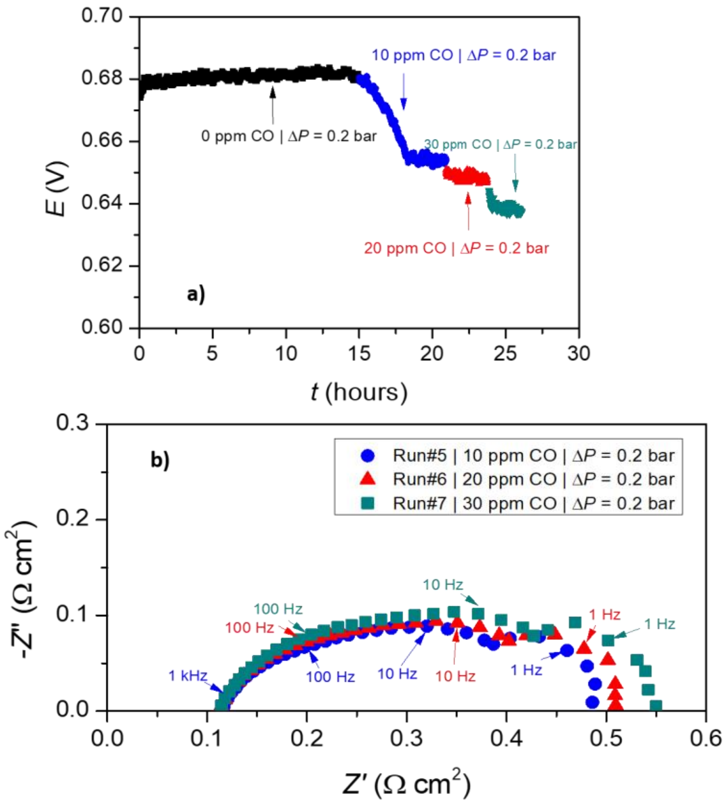

Figure 5. Effect of different CO concentrations at 500 mA cm^{-2} on a) chronopotentiometry and on b) EIS in MEA#1.

The work of Dhar [42] reported that the apparent activation energy for the HOR increases with the CO concentration thus leading to higher anode polarizations. Oetjen [43] studied the effect of different CO concentrations (25 to 250 ppm of CO) on the performance a PEMFC at 80 ºC. These authors concluded that feeding a cell with hydrogen with increasing CO contents causes a more negative slope on the polarization curve compared to that measured with pure hydrogen; this effect was more noticeable for higher current densities (> 300 mA cm^2). Similar results were already reported by other authors. [44,45].

The potential needed to oxidize hydrogen (potential range of 0 to 0.2 V) is inferior to that needed to oxidize CO (a minimum of 350 mV on Pt/Ru) [46,47]; the latter occupies the active sites following a Tempkin adsorption isotherm behaviour. If the temperature is kept constant, the CO coverage increases with its concentration in the feed, progressively blocking the active sites for the HOR resulting in lower performances [42].

3.3. External air bleeding

Figure 6a depicts the cell potential behaviour before and after introducing 10 ppm of CO together with gradually higher concentrations of air (0.5 %, 1 % and 1.5 %) in the fuel stream. 0.5 % of air is enough to cause significant gains in the performance (*ca*. 45 %) while 1.5 % of air in the anode suffices to mitigate the CO poisoning – Run #10. Figure 6b shows the EIS spectra for Runs #2, #3 and #10. Runs #2 and #10 displayed approximately the same anodic charge transfer resistance $R_a \approx 68$ mΩ cm^2 and the same series resistance $R_m \approx 217 \pm 4$ mΩ cm^2; the fuel feed of Run #10 contains 1.5 % of air (*ca*. 0.32 % of oxygen), 10 ppm of CO and the balance of hydrogen, this last from air.

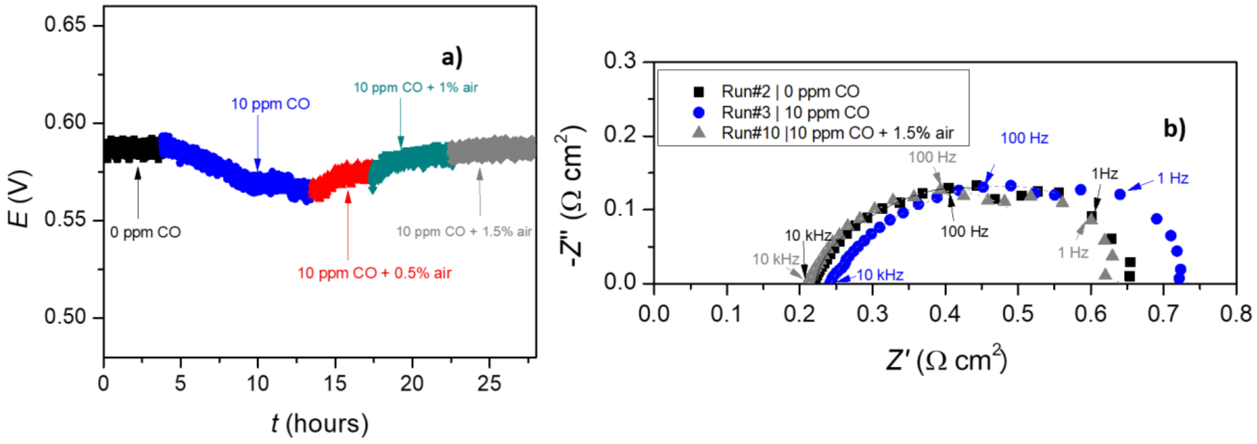

Figure 6. Effect of external bleeding at 500 mA cm^{-2} on a) chronopotentiometry and b) on EIS in MEA#1.

The effect of external air bleeding was also assessed using MEA#2. For this MEA, 1 % of air was enough to fully recover the reference potential, *cf*. Run#2 and #9 in Figure 7a. Impedance spectra for Runs #2, #3 and #9 are depicted in Figure 7b; spectra of Runs #2 and #9 overlap, confirming that the recovery from the CO poisoning was complete, in agreement with the characteristic curve results. Moreover, ohmic resistance increases when CO is added to the feed (Run #3) and returns to the reference value when external bleeding is provided (Run #9): R_m is *ca*. 125.4 mΩ cm^2 for Run #3 and R_m of 107 ± 2 mΩ cm^2 for Run #2 and #9).

Several works in the literature report that the addition of a fraction of air to a CO contaminated hydrogen stream allows the recovery of the fuel cell performance as if it was operating with pure hydrogen [48–53]. Higher CO concentrations typically require higher levels of air bleeding; for example, anode air bleeding of 15 % (*ca*. 3 % of oxygen) is not enough to fully recover the performance of a cell fed with a 53 ppm CO-contaminated hydrogen stream [54]. However, excessive air bleeding (>15 %) is dangerous and leads to the fast membrane ageing and to the decrease of the output power since a significant amount of fuel oxidizes to water at the anode side. Nevertheless, the work by Wilson and his co-workers [55] is one of the few to report the effect of external air bleeding for mitigating CO poisoning present at low concentrations. These authors reported the use of an external bleeding stream of air (2 %) for fully recover the performance of a PEMFC fed with hydrogen contaminated with 5 ppm and 20 ppm of CO; the anode was loaded with 0.14 mg cm^{-2} of PtRu. A similar work comprehended the use of an external bleeding of 6.7 % (air) for a recovery ratio of 80 % with a 10 ppm CO-contaminated hydrogen stream while using a 0.45mg cm^{-2} Pt-Ru anode [54].

The oxygen reaction with the adsorbed CO on the catalyst surface produces CO_2. As soon as the CO is oxidized and removed, the catalyst sites become available for the HOR. Here, it is reported that 1 – 1.5 % of anode air bleed is sufficient to completely recover the performance of a 10 ppm CO-contaminated fuel stream under typical operating conditions, *i.e.* m-CHP systems. To safely supply oxygen (or air) into the anode, its concentration should be kept always below the limiting oxygen concentration, which for 1 bar and room temperature is *ca*. 5 % of oxygen [56]. Furthermore, such oxygen content at the anode did not impact the open circuit potential of the cell, thus it does not contribute for lowering the PEMFC performance.

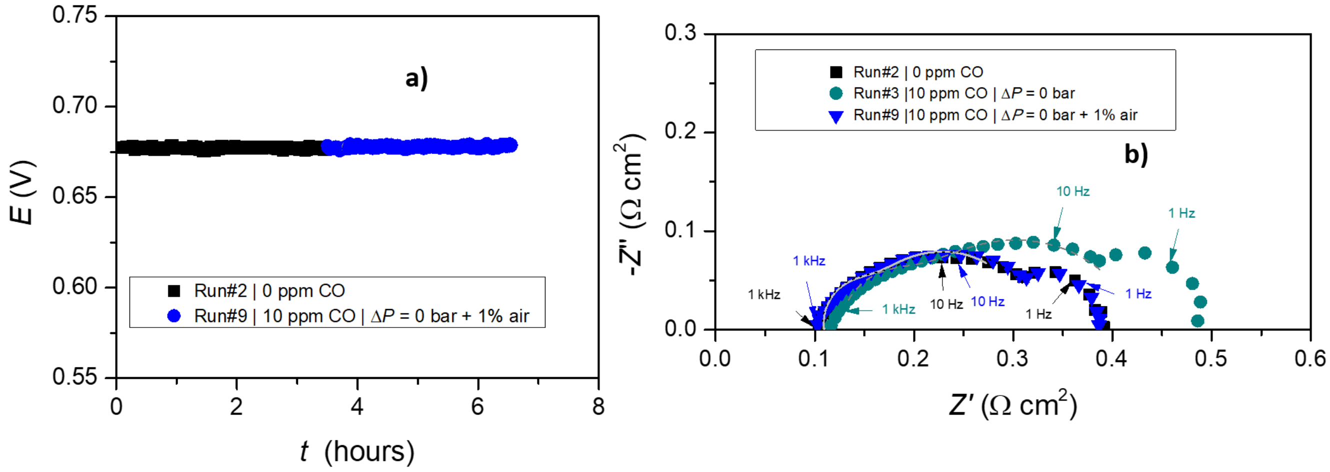

Figure 7. Effect of external air bleeding at 500 mA cm^{-2}on a) chronopotentiometry and on b) EIS in MEA#2.

3.4. Cell electrochemical stability upon implementation of bleeding strategies

Figure 8a and b compare long-term chronopotentiometries of Run #5 and Runs #9 and #10 with internal and external air bleeding, respectively, for MEA#1 and MEA#2. After reaching the steady-state potential at a current density of 500 mA·cm^{-2}, the potential loss history was recorded for assessing the long-term stability. A potential loss rate of 1.58·10^{-4} V h^{-1} is observed for an internal bleeding of 200 mbar of cathode over-pressure – Run #5 in MEA#1; on the other hand, after *ca.* 80 h of operation, MEA#2 displays a potential loss rate of 9.45·10^{-5} V h^{-1} under the same operating conditions. After *ca.* 8 h of operation the performance loss of MEA#1 under external bleeding is negligible (loss rate of *ca.* 4.30·10^{-6} V h^{-1}) – Run #10, while MEA#2 displays a potential loss rate of 8.04·10^{-5} V h^{-1} – Run #9. At reference conditions, for a CO free hydrogen feeding, the observed potential loss rate was 9.43·10^{-7} V h^{-1} for MEA#1 and 9.00·10^{-6} V h^{-1} for MEA#2. These values are quite similar to the ones obtained for the external bleeding experiments, showing that this method is not only sufficient to recover the performance of the cell but also causes less cell potential decay than internal bleeding; nonetheless, some authors have reported a detrimental effect in long-term performance when using external air bleeding due to H_2O_2 formation [16]. However, the results of demonstrate that MEA#1, that uses a thicker membrane, displays a better long-term stability even at higher air bleed concentrations than MEA#2 – 1.5 % air bleed in MEA#1 vs. 1 % of air in MEA#2.

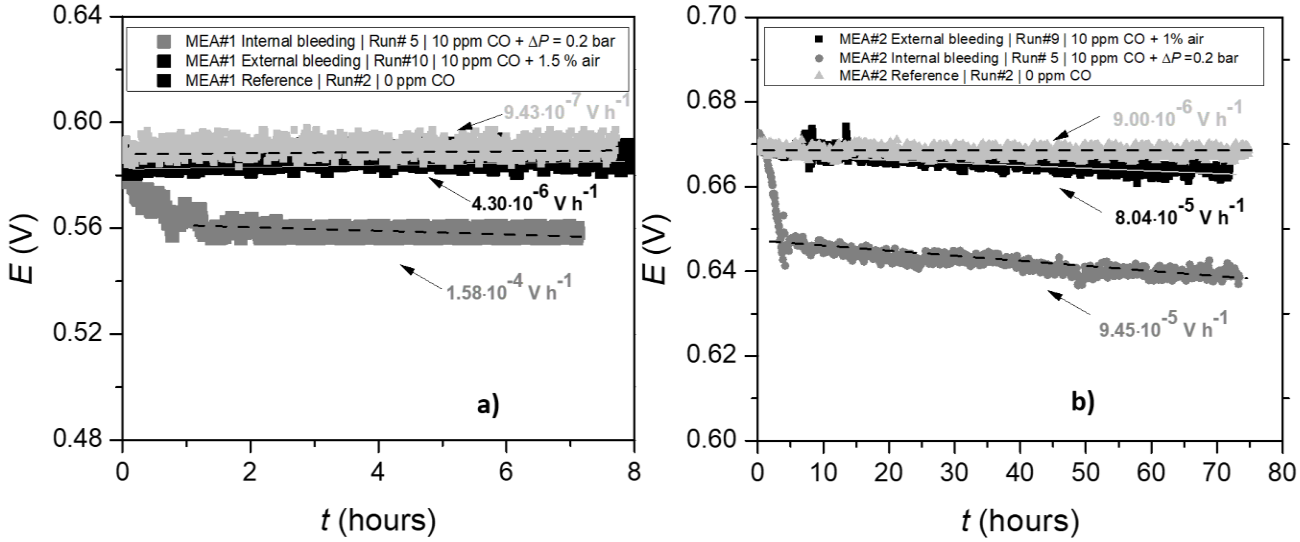

Figure 8. Long-term chronopotentiometry of two types of air bleeding at 500 mA cm^{-2} in a) MEA#1 and b) MEA#2.

Cyclic voltammetry was performed to assess the impact of CO contamination over both anode and cathode ECSA after a complete set of experiments (Runs# 3 to 9) with MEA#2. Figure 9a and b depict the BoL CV, and the end of life (EoL) CV for the anode and cathode of MEA#2, respectively. The CVs present distinct shapes due to the different catalysts used in each electrode. The peak areas reflect the number of Pt active sites to hydrogen adsorption/desorption. The anode CVs display solely one peak typical of Pt-Ru catalysts [57]. On the other hand, the cathode displays two peaks at the anodic currents region ($i > 0$) accounting for the H desorption on Pt (111) at ~ 110 mV and Pt(100) at ~ 215 mV [58]. The reduction process is electrochemically reversible since the difference between the anodic and cathodic peak potentials is less than 59 mV. After performing all tests involving CO coverage, the electrochemically active surface area seems to be kept intact with no signs of loss on catalytic activity,

Figure 9c. This result confirms the great stability of Pt-Ru alloy towards CO contaminated hydrogen streams [59]. Moreover, Wagner and Schulze [60] confirmed by EIS analysis the excellent properties of Pt-Ru/C anodes as CO-tolerant electrocatalysts for the HOR; not only do they provide less anodic charge transfer resistance but also generate less mass transfer resistance compared to Pt/C based anodes. However, there is an evident loss of active surface area of Pt at the cathode, nearly 16 %, due to the typical catalyst layer degradation that comprehends Pt dissolution/sintering, carbon corrosion and ionomer dissolution [61].

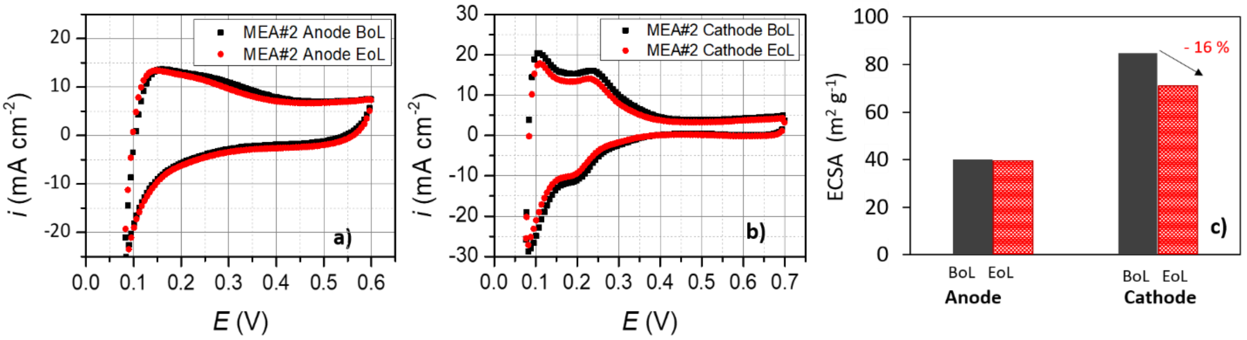

Figure 9. Cyclic voltammograms at beginning of life (BoL) and end of life (EoL) of the **a)** anode and **b)** cathode of MEA#2; scan rate: 50 mV·s^{-1}; RH: 50 %; Stoic.: 1.5/2 (H_2/O_2) at 100 mL·min^{-1}).

4. CONCLUSIONS

In the present study, the performance of PEMFCs was evaluated while feeding H_2 and CO (10 ppm) to a Pt-Ru based anode and compared with the performance with pure hydrogen at 70 °C. Oxygen concentrations were tuned and applied to the anode – by means of internal air or external air bleeding - to assess the minimum concentration to mitigate CO poisoning. Simultaneously, the long-term stability of the cells was monitored to ascribe the potential decay with each air bleeding strategy.

The potential drop caused by feeding H_2 contaminated with 10 ppm of CO was 3 % at 500 mA·cm^{-2} for the fuel cells equipped with Nafion HP membrane and a Nafion 212 membrane; nonetheless, the dynamic response to the addition of 10 ppm of CO was slow, reaching the new steady state performance after *ca*. 5 h. The air feed over-pressure of 0.2 bar at the cathode allowed the re-activation of the poisoned catalyst and a cell potential recovery of over 30 % in both MEAs. The success of internal bleeding towards CO oxidation along with the stability was found to depend on the mechanical strength of each membrane that equipped the MEAs. Thinner but reinforced and stabilized Nafion HP membrane displayed lower performance recovery but higher stability during mid-term diagnosis, in contrast to the non-reinforced and thicker Nafion 212 membrane.

Performing external air bleeding proved to be the most effective approach. In fact, adding an air bleed of 1 % and 1.5 % in the fuel stream for both MEAs promoted full CO oxidation and thus nearly 100 % recovery of cell performance (comparing to neat hydrogen). Accordingly, up to 1.5 % of air in the anode side showed to be harmless for long-term operation. This strategy is then recommendable for stationary applications, namely for residential power generation, whenever the feeding hydrogen contains up to *ca*. 10 ppm.

ACKNOWLEDGEMENTS

The authors acknowledge the financial support from the project UID/EQU/00511/2019 - Laboratory for Process Engineering, Environment, Biotechnology and Energy – LEPABE funded by national funds through FCT/MCTES (PIDDAC) and PEMFC-SUDOE - nº SOE1/P1/E0293 funded by FEDER funds through COMPETE2020 - Programa Operacional Competitividade e Internacionalização (POCI) and Programa Operacional Regional do Norte (NORTE2020) and by national funds (PIDDAC) through FCT/MCTES.

References

1. J. Tjønnås, F. Zenith, I.J. Halvorsen, M. Klages, J. Scholta, *IFAC-PapersOnLine*, 49 (2016) 302–307.
2. C.A. Rice, P. Urchaga, A.O. Pistono, B.W. McFerrin, B.T. McComb, J. Hu, *J. Electrochem. Soc.*, 162 (2015) F1175–F1180.
3. S. Foresti, G. Manzolini, S. Escribano, *Int. J. Hydrogen Energy*, 42 (2017) 25334–25350.
4. T.J. Park, S.M.; O'Brien, Effects of Several Trace Contaminants on Fuel Cell Performance, (1979).
5. N. Hayter, P R; Mitchell, P; Dams, R A.J.; Dudfield, C; Gladding, The Effect of Contaminants in the Fuel and Air Streams on the Performance of a Solid Polymer Fuel Cell, (1997).
6. P.E. Dodds, I. Staffell, A.D. Hawkes, F. Li, P. Grünewald, W. McDowall, P. Ekins, *Int. J. Hydrogen Energy*, 40 (2015) 2065–2083.
7. I. Staffell, *Appl. Energy*, 147 (2015) 373–385.
8. R.A. Lemons, *J. Power Sources*, 29 (1990) 251–264.
9. H. Igarashi, T. Fujino, M. Watanabe, *J. Electroanal. Chem.*, 391 (1995) 119–123.
10. X. Cheng, Z. Shi, N. Glass, L. Zhang, J. Zhang, D. Song, Z.S. Liu, H. Wang, J. Shen, *J. Power Sources*, 165 (2007) 739–756.
11. Z. Qi, C. He, A. Kaufman, *J. Power Sources*, 111 (2002) 239–247.
12. R.J. Bellows, E.M. Soos, R.P. Reynolds, *Electrochem. Solid-State Lett.*, 1 (1999) 69.
13. L.P.L. Carrette, K.A. Friedrich, M. Huber, U. Stimming, Phys. Chem. Chem. Phys., (2001).
14. C.-C. Chung, C.-H. Chen, D.-Z. Weng, *Appl. Therm. Eng.*, 29 (2009) 2518–2526.
15. R. Bashyam, P. He, S. Wessel, S. Knights, ECS Trans., (2011).
16. S. Knights, R. Bashyam, P. He, M. Lauritzen, C. Startek, V. Colbow, T. Cheng, J. Kolodziej, S. Wessel, *ECS Trans.*, 41 (2011) 39–53.
17. M.J. Lee, J.S. Kang, Y.S. Kang, D.Y. Chung, H. Shin, C.Y. Ahn, S. Park, M.J. Kim, S. Kim, K.S. Lee, Y.E. Sung, *ACS Catal.*, 6 (2016) 2398–2407.
18. S. Alayoglu, A.U. Nilekar, M. Mavrikakis, B. Eichhorn, *Nat. Mater.*, 7 (2008) 333–338.
19. A.H. Thomason, T.R. Lalk, A.J. Appleby, *J. Power Sources* (2004).
20. Y. Kurihara, T. Mabuchi, T. Tokumasu, *J. Electrochem. Soc.* (2017).
21. T. Kawakami, I. Shigemoto, N. Matubayasi, *J. Chem. Phys.* (2012).
22. A.T. Haug, R.E. White, *J. Electrochem. Soc.* (2000).
23. P. Gode, G. Lindbergh, G. Sundholm, *J. Electroanal. Chem.* (2002).
24. K. Lee, A. Ishihara, S. Mitsushima, N. Kamiya, K. Ota, *J. Electrochem. Soc.* (2004).
25. V.A. Sethuraman, S. Khan, J.S. Jur, A.T. Haug, J.W. Weidner, *Electrochim. Acta* (2009).
26. S.S. Kocha, J.D. Yang, J.S. Yi, *AIChE J.*, 52 (2006).
27. J. Zhang, T. Thampan, R. Datta, *J. Electrochem. Soc.* (2002).
28. M. Murthy, M. Esayian, A. Hobson, S. Mackenzie, W. Lee, J.W. Van Zee, M. Murthy,a, J.W. Van Zee, *J. Electrochem. Soc.* (2001).
29. Y. V. Pleskov, Y.E. Evstefeeva, M.D. Krotova, V. V. Elkin, A.M. Baranov, A.P. Dement'Ev, *Diam. Relat. Mater.*, 8 (1999) 64–72.
30. X.-Z. Yuan, S. Zhang, H. Wang, J. Wu, J.C. Sun, R. Hiesgen, K.A. Friedrich, M. Schulze, A.

Haug, *J. Power Sources*, 195 (2010) 7594–7599.
31. L. Yu, F. Lin, L. Xu, J. Xi, *RSC Adv.*, 7 (2017) 31164–31172.
32. DuPont Fuel Cells, DuPont^{TM} Nafion® PFSA Membranes NR-211 and NR-212, (2008).
33. DuPont Fuel Cells, (2010).
34. S. Slade, S.A. Campbell, T.R. Ralph, F.C. Walsh, *J. Electrochem. Soc.*, 149 (2002) A1556.
35. X.-Z. Yuan, S. Zhang, H. Wang, J. Wu, J.C. Sun, R. Hiesgen, K.A. Friedrich, M. Schulze, A. Haug, *J. Power Sources*, 195 (2010) 7594–7599.
36. M.N. Tsampas, A. Pikos, S. Brosda, A. Katsaounis, C.G. Vayenas, *Electrochim. Acta*, 51 (2006) 2743–2755.
37. W. Wang, *J. Power Sources*, 191 (2009) 400–406.
38. K.M. Nouel, P.S. Fedkiw, *Electrochim. Acta*, 43 (1998) 2381–2387.
39. F. Liu, B. Yi, D. Xing, J. Yu, H. Zhang, *J. Memb. Sci.*, 212 (2003) 213–223.
40. J. Shim, H.Y. Ha, S.-A. Hong, I.-H. Oh, *J. Power Sources*, 109 (2002) 412–417.
41. H.-L. Lin, T.L. Yu, L.-N. Huang, L.-C. Chen, K.-S. Shen, G.-B. Jung, *J. Power Sources*, 150 (2005) 11–19.
42. H.P. Dhar, L.G. Christner, A.K. Kush, H.C. Maru, *J. Electrochem. Soc.* , 133 (1986) 1574–1582.
43. U. Oetjen, H.-F., Schmidt, V.M , Stimming, *J. Electrochem. Soc.*, 143 (1996) 3838.
44. V.M. Schmidt, R. Ianniello, H.-F. Oetjen, H. Reger, U. Stinuning, F. Trila, *ECS Proc. Vol.* , 1995–23 (1995) 1–11.
45. Y. Si, R. Jiang, J.-C. Lin, H.R. Kunz, J.M. Fenton, *J. Electrochem. Soc.*, 151 (2004) A1820–A1824.
46. Y. Takasu, T. Kawaguchi, W. Sugimoto, Y. Murakami, *Electrochim. Acta*, 48 (2003) 3861–3868.s
47. T. Gu, W.-K. Lee, J.W. Van Zee, M. Murthy, *J. Electrochem. Soc.*, 151 (2004) A2100–A2105.
48. L.Y. Sung, B.J. Hwang, K.L. Hsueh, F.H. Tsau, *J. Power Sources*, 195 (2010) 1630–1639.
49. T. Tingelöf, L. Hedström, N. Holmström, P. Alvfors, G. Lindbergh, *Int. J. Hydrogen Energy*, 33 (2008) 2064–2072.
50. L.Y. Sung, B.J. Hwang, K.L. Hsueh, W.N. Su, C.C. Yang, *J. Power Sources*, 242 (2013) 264–272.
51. F.A. Uribe, J.A. Valerio, F.H. Garzon, T.A. Zawodzinski, *Electrochem. Solid-State Lett.*, 7 (2004) A376–A379.
52. R.C. Urian, A.F. Gullá, S. Mukerjee, *J. Electroanal. Chem.*, 554–555 (2003) 307–324.
53. T. Morawietz, M. Handl, C. Oldani, K.A. Friedrich, R. Hiesgen, *ACS Appl. Mater. Interfaces*, 40 (2016) 27044–27054.
54. X. Cheng, Z. Shi, N. Glass, L. Zhang, J. Zhang, D. Song, Z.-S. Liu, H. Wang, J. Shen, *J. Power Sources*, 165 (2007) 739–756.
55. S.F.. Wilson, M.S., Derouin, C.R., Valerio, J.A., and Gottesfeld, Conf. 28. Intersoc. Energy Convers. Eng. Conf. Atlanta, GA (United States), 8-13 Aug 1993, (1193).
56. I.A. Zlochower, G.M. Green, *J. Loss Prev. Process Ind.*, 22 (2009) 499–505.
57. S.J. Yoo, T.Y. Jeon, K.S. Kim, T.H. Lim, Y.E. Sung, *Phys. Chem. Chem. Phys.*, 46 (2010) 15240–15246.
58. W. Sheng, Z. Zhuang, M. Gao, J. Zheng, J.G. Chen, Y. Yan, *Nat. Commun.*, 6 (2015) 5848.
59. H.-F. Oetjen, *J. Electrochem. Soc.* (1996).
60. N. Wagner, M. Schulze, *Electrochim. Acta*, 48 (2003) 3899–3907.
61. X. Yu, S. Ye, *J. Power Sources*, 172 (2007) 145–154.